AIAA–2000–0475
Noise Computation of a Shock-Containing Supersonic Axisymmetric Jet by the CE/SE Method

Ching Y. Loh
Taitech Inc.
Cleveland, OH
and
Lennart S. Hultgren, Sin-Chung Chang, and
Philip C.E. Jorgenson
NASA Glenn Research Center
Cleveland, OH

38th Aerospace Sciences Meeting & Exhibit
January 10–13, 2000 / Reno, NV

NASA/TM—1999-209658 AIAA–2000–0475

Noise Computation of a Shock-Containing Supersonic Axisymmetric Jet by the CE/SE Method

Ching Y. Loh
Taitech Inc., Cleveland, Ohio

Lennart S. Hultgren, Sin-Chung Chang, and Philip C.E. Jorgenson
Glenn Research Center, Cleveland, Ohio

December 1999

The NASA STI Program Office . . . in Profile

Since its founding, NASA has been dedicated to the advancement of aeronautics and space science. The NASA Scientific and Technical Information (STI) Program Office plays a key part in helping NASA maintain this important role.

The NASA STI Program Office is operated by Langley Research Center, the Lead Center for NASA's scientific and technical information. The NASA STI Program Office provides access to the NASA STI Database, the largest collection of aeronautical and space science STI in the world. The Program Office is also NASA's institutional mechanism for disseminating the results of its research and development activities. These results are published by NASA in the NASA STI Report Series, which includes the following report types:

- TECHNICAL PUBLICATION. Reports of completed research or a major significant phase of research that present the results of NASA programs and include extensive data or theoretical analysis. Includes compilations of significant scientific and technical data and information deemed to be of continuing reference value. NASA's counterpart of peer-reviewed formal professional papers but has less stringent limitations on manuscript length and extent of graphic presentations.

- TECHNICAL MEMORANDUM. Scientific and technical findings that are preliminary or of specialized interest, e.g., quick release reports, working papers, and bibliographies that contain minimal annotation. Does not contain extensive analysis.

- CONTRACTOR REPORT. Scientific and technical findings by NASA-sponsored contractors and grantees.

- CONFERENCE PUBLICATION. Collected papers from scientific and technical conferences, symposia, seminars, or other meetings sponsored or cosponsored by NASA.

- SPECIAL PUBLICATION. Scientific, technical, or historical information from NASA programs, projects, and missions, often concerned with subjects having substantial public interest.

- TECHNICAL TRANSLATION. English-language translations of foreign scientific and technical material pertinent to NASA's mission.

Specialized services that complement the STI Program Office's diverse offerings include creating custom thesauri, building customized data bases, organizing and publishing research results . . . even providing videos.

For more information about the NASA STI Program Office, see the following:

- Access the NASA STI Program Home Page at ***http://www.sti.nasa.gov***

- E-mail your question via the Internet to help@sti.nasa.gov

- Fax your question to the NASA Access Help Desk at (301) 621-0134

- Telephone the NASA Access Help Desk at (301) 621-0390

- Write to:
  NASA Access Help Desk
  NASA Center for AeroSpace Information
  7121 Standard Drive
  Hanover, MD 21076

NASA/TM—1999-209658 AIAA–2000–0475

Noise Computation of a Shock-Containing Supersonic Axisymmetric Jet by the CE/SE Method

Ching Y. Loh
Taitech Inc., Cleveland, Ohio

Lennart S. Hultgren, Sin-Chung Chang, and Philip C.E. Jorgenson
Glenn Research Center, Cleveland, Ohio

Prepared for the
38th Aerospace Sciences Meeting and Exhibit
sponsored by the American Institute of Aeronautics and Astronautics
Reno, Nevada, January 10–13, 2000

National Aeronautics and
Space Administration

Glenn Research Center

December 1999

Available from

NASA Center for Aerospace Information
7121 Standard Drive
Hanover, MD 21076
Price Code: A03

National Technical Information Service
5285 Port Royal Road
Springfield, VA 22100
Price Code: A03

NOISE COMPUTATION OF A SHOCK-CONTAINING SUPERSONIC AXISYMMETRIC JET BY THE CE/SE METHOD

Ching Y. Loh,* Lennart S. Hultgren,† Sin-Chung Chang,‡ and Philip C.E. Jorgenson§
National Aeronautics and Space Administration
Glenn Research Center
Cleveland, Ohio 44135, USA

Abstract

The space-time conservation element solution element (CE/SE) method [1] is employed to numerically study the near-field of a typical under-expanded jet. For the computed case—a circular jet with Mach number $M_j = 1.19$—the shock-cell structure is in good agreement with experimental results [2, 3]. The computed noise field is in general agreement with the experiment, although further work is needed to properly close the screech feedback loop.

1 Introduction

An under-expanded supersonic jet radiates mixing noise, broadband shock-associated noise, as well as screech tones under certain conditions. These complicated and technologically important physical phenomena have been the topic of many experimental and theoretical investigations, see Tam's review paper [4] for a comprehensive list of references. Simply put, the mixing noise is directly associated with large-scale structures, or instability waves, in the jet shear layer, whereas the broadband shock-associated noise and screech tones are associated with the interaction of these waves with the shock-cell structure in the jet core. The distinct screech tones arise due to a feedback loop, *i.e.*, part of the acoustic waves generated by the wave/shock-cell interaction propagate upstream and re-generate the instability waves at, or in the vicinity of, the nozzle lip. More details can be found in the review papers [4-7] and the references therein. Screech tones are of particular interest not only because of general noise-reduction concerns, but also because of potentially destructive structural interaction(s) leading to sonic fatigue. The feedback loop leading to screech tones is very sensitive to small changes in the system conditions and the understanding of the phenomena is to date mostly based on experimental observations, e.g. [2, 3]. A modular simulation tool has been developed at McDonnell Douglas Aerospace, with components approximating the relevant physics, allowing designers to reasonably well estimate jet screech tones, see [7-9] for further details. Recently, Shen and Tam [10] obtained good results in a direct numerical simulation of screech for a (low) supersonic Mach number axisymmetric jet.

Jet noise is a challenging topic in computational aeroacoustics, in particular, near-field noise computation in the presence of shock cells in the jet core. In this situation, the computational scheme is required on one hand to resolve the acoustic waves without introducing too much dispersion error and numerical dissipation, while on the other hand, it is required to capture shocks, or other nonlinear phenomena, near or inside the jet correctly. In addition, non-reflecting boundary conditions must be implemented, which is more difficult to accomplish in the near field than in the far field.

The recent 'Space-Time Conservation Element and Solution Element Method' [11], or the CE/SE method in short, is a scheme that meets the above requirements. The CE/SE scheme possesses attractive properties for aeroacoustics computations in that: (*i*) it possesses low dispersion and dissipation errors; (*ii*) its 'built-in' shock-capturing nature makes the computation of shock-cell structures simple and accurate; (*iii*) the non-reflecting boundary conditions are simple and effective and can be applied in the near field of the jet without introducing excessive errors; and (*iv*) the scheme delivers the design accuracy for the vorticity, which plays an important role in the noise generating mechanism. A detailed description of the CE/SE method can be found in the reports of Chang *et al* [12,13]. As demonstrated in our previous papers, the CE/SE scheme is well suited for computing waves on compressible shear

*Taitech Inc., Member AIAA
†Associate Fellow AIAA
‡Member AIAA
§Member AIAA

flows [14] as well as vorticity/shock interactions [14, 15], both being corner stones of the jet-noise phenomena.

In this paper, the near-field noise of a shock-containing axisymmetric supersonic jet is investigated numerically by using a CE/SE Euler solver. The paper is arranged as follows: The axisymmetric CE/SE scheme is briefly discussed in Section 2. Section 3 illustrates the initial and boundary conditions for the jet-noise problem, in particular, the novel non-reflecting boundary conditions which are based on *flux balance*. The numerical results are presented and compared to experimental findings [2, 3] in Section 4. Conclusions are given in Section 5.

2 Axisymmetric CE/SE Euler Method

In general, the CE/SE method systematically solves a set of *integral* equations derived directly from the physical conservation laws. Because of its integral formulation and since, as will be seen below, space and time are treated 'on the same footing', the scheme naturally captures shocks and other discontinuities in the flow. Both dependent variables and their derivatives are solved for simultaneously and, consequently, the flow vorticity can be obtained without reduction in accuracy. Non-reflective boundary conditions are also easily implemented because of the flux-conservation formulation.

2.1 Conservation Form of the Unsteady Axisymmetric Euler Equations

Consider a dimensionless conservation form of the unsteady axisymmetric Euler equations of a perfect gas. Let ρ, u, v, p, and γ be the density, streamwise velocity component, radial velocity component, static pressure, and constant specific heat ratio, respectively. The axisymmetric Euler equations then can be written in the following vector form:

$$\boldsymbol{U}_t + \boldsymbol{F}_x + \boldsymbol{G}_y = \boldsymbol{Q}. \qquad (1)$$

where x, $y \geqslant 0$, and t are the streamwise and radial coordinates and time, respectively, and the conservative flow variable vector $\boldsymbol{U}$ and the flux vectors in the streamwise and radial directions, $\boldsymbol{F}$ and $\boldsymbol{G}$, are given by:

$$\boldsymbol{U} = \begin{pmatrix} U_1 \\ U_2 \\ U_3 \\ U_4 \end{pmatrix}, \quad \boldsymbol{F} = \begin{pmatrix} F_1 \\ F_2 \\ F_3 \\ F_4 \end{pmatrix}, \quad \boldsymbol{G} = \begin{pmatrix} G_1 \\ G_2 \\ G_3 \\ G_4 \end{pmatrix},$$

with

$$U_1 = \rho, \quad U_2 = \rho u, \quad U_3 = \rho v,$$
$$U_4 = p/(\gamma - 1) - \rho(u^2 + v^2)/2$$

$$F_1 = U_2,$$
$$F_2 = (\gamma - 1)U_4 + \left[(3 - \gamma)U_2^2 - (\gamma - 1)U_3^2\right]/2U_1,$$
$$F_3 = U_2U_3/U_1,$$
$$F_4 = \gamma U_2U_4/U_1 - (\gamma - 1)U_2\left[U_2^2 + U_3^2\right]/2U_1^2,$$
$$G_1 = U_3, \quad G_2 = U_2U_3/U_1,$$
$$G_3 = (\gamma - 1)U_4 + \left[(3 - \gamma)U_3^2 - (\gamma - 1)U_2^2\right]/2U_1,$$
$$G_4 = \gamma U_3U_4/U_1 - (\gamma - 1)U_3\left[U_2^2 + U_3^2\right]/2U_1^2,$$

and

$$\boldsymbol{Q} = \begin{pmatrix} Q_1 \\ Q_2 \\ Q_3 \\ Q_4 \end{pmatrix},$$

with

$$Q_1 = -U_3/y, \quad Q_2 = -U_2U_3/U_1y,$$
$$Q_3 = -U_3^2/U_1y, \quad Q_4 = -G_4/y.$$

The axisymmetric Euler equations can be though of in this formulation as a variation of their two-dimensional counter parts with 'source' terms on their right-hand sides.

By considering (x, y, t) as coordinates of a three-dimensional Euclidean space E_3 and using Gauss' divergence theorem, it follows that Eq. (1) is equivalent to the following integral conservation law:

$$\oint_{S(V)} \boldsymbol{H}_m \cdot \mathrm{d}\mathbf{S} = \int_V Q_m \mathrm{d}V, \qquad m = 1, 2, 3, 4. \quad (2)$$

where $S(V)$ denotes the surface around a volume V in E_3 and $\boldsymbol{H}_m = (F_m, G_m, U_m)$.

2.2 CE/SE Structure

In the CE/SE scheme, the flux conservation relation in space-time is the *only* mechanism that transfers information between node points. The conservation element CE, or computational cell, is the finite volume to which the integral flux condition (2) is to be applied. Discontinuities are allowed to occur in the interior of a conservation element as long as the integrals on the right-hand side of (2) exist. A solution element SE associated with a grid node is here a set of three interface planes in E_3 that passes through this node. The solution, *i.e.* $\boldsymbol{U}$, $\boldsymbol{U}_x$, and $\boldsymbol{U}_y$ are calculated at this node. Within a given solution element $SE(j, k, n)$, where (j, k, n) is the node index, the flow variables are not only considered continuous but are also approximated by linear Taylor expansions:

$$\boldsymbol{U}^*(x, y, t; j, k, n) = \boldsymbol{U}_{j,k}^n + (\boldsymbol{U}_x)_{j,k}^n(x - x_{j,k}) -$$

$$(\boldsymbol{U}_y)^n_{j,k}(y-y_{j,k})+(\boldsymbol{U}_t)^n_{j,k}(t-t^n). \quad (3)$$

$$\boldsymbol{F}^*(x,y,t;j,k,n)=\boldsymbol{F}^n_{j,k}+(\boldsymbol{F}_x)^n_{j,k}(x-x_{j,k})+$$
$$(\boldsymbol{F}_y)^n_{j,k}(y-y_{j,k})+(\boldsymbol{F}_t)^n_{j,k}(t-t^n), \quad (4)$$

$$\boldsymbol{G}^*(x,y,t;j,k,n)=\boldsymbol{G}^n_{j,k}+(\boldsymbol{G}_x)^n_{j,k}(x-x_{j,k})+$$
$$(\boldsymbol{G}_y)^n_{j,k}(y-y_{j,k})+(\boldsymbol{G}_t)^n_{j,k}(t-t^n). \quad (5)$$

where the partial derivatives of $\boldsymbol{F}$ and $\boldsymbol{G}$ can be related to the corresponding one of $\boldsymbol{U}$ by using the chain rule and $\boldsymbol{U}_t$ can be obtained from (1).

The discrete approximation of (2) is then

$$\oint_{S(CE)} \boldsymbol{H}^*_m \cdot d\mathbf{S} = V(CE) \sum_{(j,k,n)\in S(CE)} \mathcal{B}^n_{j,k}(Q_m)^n_{j,k}, \quad (6)$$

for $m = 1,2,3$, where $\boldsymbol{H}^*_m = (F^*_m, G^*_m, U^*_m)$ and $\sum_{(j,k,n)\in S(CE)} \mathcal{B}^n_{j,k} = 1$. The right-hand side of (6), in general, is the volume of the CE times a weighted average of the 'source' term evaluated at the nodes on $S(CE)$. Each $S(CE)$ is made up by surface segments belonging to *two* neighboring SE's. All the unknowns are solved for based on these relations. No extrapolations (interpolations) across a stencil of cells are needed or allowed.

In order that the number of equations derived from the flux conservation law above matches the number of unknowns (here 12 scalar unknowns), the grid needs to be carefully designed [11, 13]. The mesh is staggered in both time and space. In a spatial plane in E_3, the grid nodes, see Fig. 1, are grouped as two staggered sets Ω_1 (open circles) and Ω_2 (filled circles). At a given time step the unknowns are evaluated only on one of the grid sets, Ω_1 or Ω_2, and at the next it will be evaluated on the other set, i.e., the spatial sets alternate as time is stepped forward. As can be seen in this figure, each 'interior' node point then has three nearest neighbors at the previous time step. Thus, there are three CE's associated with each node point in this arrangement and, therefore, there are the same number of relations as there are unknowns. Fig. 2 illustrates the three conservation elements associated with a node point and its three nearest neighbors at the previous time step. Because of the staggered spatial grids, the method can be thought of as a 'two-step' method in time.

2.3 Treatment of the Source Term

In solving (6), only the $\mathcal{B}^n_{j,k}$ corresponding to the new (half) time level is taken to be nonzero (and equal to unity). This strategy has successfully been applied by Yu *et al* [16] to problems with very stiff source terms.

As the source term $\boldsymbol{Q} = \boldsymbol{Q}(\boldsymbol{U})$ itself is a function of the unknown $\mathbf{U}$ at the new (half) time level, a local iterative procedure is needed to determine $\mathbf{U}$. For our particular choice of $\mathcal{B}^n_{j,k}$, the discretized integral equation (6) reduces to the form

$$\mathbf{U} - \mathbf{Q}(\mathbf{U})\frac{\Delta t}{2} = \mathbf{U}_H. \quad (7)$$

where $\boldsymbol{U}_H$ is the local homogeneous solution ($\boldsymbol{Q} = 0$ locally). Note that $\boldsymbol{U}_H$ only depends on the solution at the previous (half) time step, *i.e.* $\boldsymbol{U}_H$ is obtained using explicit formulas. A Newton iterative procedure to determine $\boldsymbol{U}$ is then

$$\boldsymbol{U}^{(i+1)} = \boldsymbol{U}^{(i)} - (\frac{\partial \boldsymbol{\Phi}}{\partial \boldsymbol{U}})^{-1}[\boldsymbol{\Phi}(\boldsymbol{U}^{(i)}) - \boldsymbol{U}_H],$$

where i is the iteration number and

$$\boldsymbol{\Phi}(\boldsymbol{U}) = \boldsymbol{U} - \boldsymbol{Q}(\boldsymbol{U})\frac{\Delta t}{2}.$$

Normally, $\boldsymbol{U}$ at the previous (full) time step is a good initial guess $\mathbf{U}^{(0)}$ and the procedure takes about 2-3 iterations to convergence. The Jacobian matrix is given by

$$\frac{\partial \boldsymbol{\Phi}}{\partial \boldsymbol{U}} = \begin{pmatrix} 1 & 0 & \frac{\Delta t}{2y} & 0 \\ -\frac{U_2U_3\Delta t}{2U_1^2y} & 1+\frac{U_3\Delta t}{2U_1y} & \frac{U_2\Delta t}{2U_1y} & 0 \\ -\frac{U_3^2\Delta t}{2U_1^2y} & 0 & 1-\frac{U_3\Delta t}{2U_1y} & 0 \\ A_1 & A_2 & A_3 & 1+\frac{\gamma U_3\Delta t}{2U_1y} \end{pmatrix},$$

where

$$A_1 = -\frac{U_3\Delta t}{2U_1y}[\gamma U_1 - \frac{(\gamma-1)(U_2^2+U_3^2)}{U_1}],$$

$$A_2 = -(\gamma-1)\frac{U_2U_3\Delta t}{2U_1^2y},$$

$$A_3 = \frac{\Delta t}{2y}[-\frac{\gamma-1}{2}\frac{U_2^2+3U_3^2}{U_1^2} + \frac{\gamma U_1}{U_1}].$$

The inverse of the Jacobian, i.e., $(\frac{\partial \boldsymbol{\Phi}}{\partial \mathbf{U}})^{-1}$ can easily be derived analytically for this particular case, thus, leading to savings in CPU time.

3 The Jet-Noise Problem

Consider a circular jet as sketched in Fig. 3. The flow inside the sonic jet nozzle is a choked flow with exit Mach number $M_e = 1$, while outside the nozzle in the jet, the Mach number is $M_j = 1.19$, and the ambient flow around the jet is stationary. These conditions correspond to the experimental setup of Panda [2, 3]. In his experiments, it was shown that for the above $M_j = 1.19$, the jet noise field is in

an axisymmetric mode. Hence, the axisymmetric CE/SE code described above is appropriate for computation at these conditions.

In this investigation, our attention is focussed on the near field of the jet nozzle since this is the source region for aeroacoustic noise. The diameter D of the jet nozzle is chosen as the length scale. The computational domain is a circular cylinder of $12D$ axial length and $5D$ radius. The grid currently used is a uniform one and the numbers of nodes in the x and y directions are 301 and 401, respectively, since good grid resolution is needed in the jet shear layer. The computational domain is about the same size as the experimental one in the radial direction but it is about twice as long in the axial direction. The computational scheme is of the α-ϵ type [12,13] with $\alpha = 0$ and $\epsilon = 0.5$.

3.1 General Initial Conditions

As shown in Fig. 3, there are four regions in the experiment, namely, the plenum, the convergent nozzle with choked flow, the jet core area, and the surrounding ambient flow area. Only the latter two regions (III and IV in the figure) are included in the computational domain. A conceivable initial condition is to assume that the pressure is uniform in the entire computational domain and equal to the ambient pressure, except at the jet nozzle exit where a higher pressure p_e is imposed since the jet is underexpanded. We will also make the reasonable assumption that the temperature in the plenum equals the ambient one.

Let the density, axial velocity, and temperature in the jet core, be the scales for the dependent variables. Hence, the initial conditions in the jet core are given by

$$\rho_j = 1, \quad T_j = 1, \quad u_j = 1, \quad v_j = 0, \quad p_j = \frac{1}{\gamma M_j^2},$$

where T denotes the temperature. The initial conditions in the ambient region are given by

$$\rho_a = 1/T_a, \quad T_a = 1 + \tfrac{1}{2}(\gamma - 1)M_j^2,$$

$$u_a = 0, \quad v_a = 0, \quad p_a = \frac{1}{\gamma M_j^2},$$

where the result for the temperature follows from the assumptions of constant total enthalpy in the jet flow and that the plenum and ambient temperatures are equal.

By using the assumption of constant total enthalpy and the condition for isentropic flow, it follows that the pressure p_e at the nozzle exit can be related to the pressure p_j in the jet core, thus, yielding

$$\frac{p_e}{p_j} = \left[\frac{1 + \frac{1}{2}(\gamma - 1)M_j^2}{1 + \frac{1}{2}(\gamma - 1)M_e^2}\right]^{\frac{\gamma}{\gamma - 1}}.$$

3.2 Initial Shear Layer Assumptions

The ambient and jet core regions are connected by a continuously changing shear layer. In the present numerical computations, two distinct types of initial shear layers were assumed and it was found, as will be seen below, that the results were somewhat sensitive to this choice.

3.2.1 Parallel Shear Layer The shear layer is assumed to be of constant thickness and is taken to be a hyperbolic-tangent one.

$$u(y) = \tfrac{1}{2}[1 - \tanh 20(y - \tfrac{1}{2})].$$

With the Prandtl number taken as unity for simplicity, the temperature in the shear layer is then given by the Busemann-Crocco's relation

$$T(y) = T_a + (1 - T_a)u - \tfrac{1}{2}(\gamma - 1)M_j^2 u(1 - u),$$

which in this case reduces to

$$T(y) = 1 + \tfrac{1}{2}(\gamma - 1)M_j^2(1 - u^2).$$

The density profile in the shear layer is simply given by $\rho(y) = 1/T(y)$.

3.2.2 Artificially Expanded Shear Layer The empirical quasi-parallel shear-layer profile described by Morris and Tam [17] for a fully expanded jet is imposed as the initial condition. This shear layer has a constant pressure and zero radial velocity, but the axial velocity depends weakly on the axial coordinate through slow changes in the mixing layer width b, the radius of the potential core h, and, ultimately, the core velocity u_c.

$$u = u_c, \ y \leqslant h: \quad u = u_c \exp[-\ln 2\,(\frac{y - h}{b})^2], \ y \geqslant h;$$

where

$$u_c = 1, \ x \leqslant x_c: \quad u_c = 1 - \exp(\frac{1.35}{1 - x/x_c}), \ x \geqslant x_c;$$

$$b = \frac{1.2658x}{10.7}(1 - .273M_j^2). \quad x_c = 4.2 - 1.1M_j^2.$$

x_c is the length of the potential core. The radius of the potential core, h, is determined by considering the conservation of axial momentum. After u is determined, the density ρ can be obtained as above.

3.3 Boundary Conditions

At the inlet boundary, the dependent variables and their spatial derivatives are specified to be those of the ambient flow, except at the nozzle exit, $0 \leqslant y \leqslant \frac{1}{2}$, where the elevated pressure $p = p_e$ is imposed, *i.e.* the jet is under-expanded, as in the physical experiment.

An artificial forcing of the shear layer is also introduced at the lip of the nozzle through a small perturbation in the radial velocity component,

$$v'(x = 0) = \delta \sin(2\pi St) \exp[-(y - \tfrac{1}{2})^2],$$

in order to organize the flow somewhat and to provide a reference signal for conditional sampling of the computed results. The amplitude $\delta = 0.001$ is, in general, used throughout this study and the Strouhal number, or nondimensional frequency, $St = 0.59$ corresponds to the experimentally observed screech tone.

At $y = 0$, the appropriate conditions are applied which can be deduced from the limiting form of Eq. (1) as $y \to 0$. At the top and outflow boundaries, the Type I and Type II CE/SE non-reflecting boundary conditions as described in the next subsection are imposed respectively.

3.4 Non-Reflecting Boundary Conditions

In the CE/SE scheme, non-reflective boundary conditions are constructed so as to allow fluxes from the interior domain to a boundary CE smoothly exit to the exterior of the domain. There are various variants of the non-reflecting boundary condition and in general they have proven to be well suited for aeroacoustic problems [18-23]. The following are the ones employed in this paper.

For a grid node (j, k, n) lying at the outer radius of the domain the non-reflective boundary condition (type I) requires that

$$(\boldsymbol{U}_x)^n_{j,k} = (\boldsymbol{U}_y)^n_{j,k} = 0,$$

while $\boldsymbol{U}^n_{j,k}$ is kept fixed at the initially given steady boundary value. At the downstream boundary, where there are substantial gradients in the radial direction, the non-reflective boundary condition (type II) requires that

$$(\boldsymbol{U}_x)^n_{j,k} = 0.$$

while $\boldsymbol{U}^n_{j,k}$ and $(\boldsymbol{U}_y)^n_{j,k}$ are now defined by simple extrapolation from the interior, *i.e.*,

$$\boldsymbol{U}^n_{j,k} = \boldsymbol{U}^{n-1/2}_{j',k'} \quad (\boldsymbol{U}_y)^n_{j,k} = (\boldsymbol{U}_y)^{n-1/2}_{j',k'}.$$

4 Numerical Results

In this section, the numerical results for the axisymmetric under-expanded circular jet are presented and compared to experimental results [2, 3]. At the low supersonic jet Mach number $M_j = 1.19$ and the exit pressure to ambient pressure ratio $p_e/p_a = 1.2645$, the overall motion in the experiment [2] is in an axisymmetric mode and with a screech tone at the Strouhal number $St = 0.59$. For imperfectly expanded jets such as this one, a quasi-periodic shock-cell structure is formed in the jet plume. The streamwise-growing instability waves naturally occurring in the jet shear layer interacts with this shock-cell structure and generate broadband shock-associated noise and under certain conditions screech tones through a feedback loop.

It is important to realize that even if no harmonic forcing is intentionally imposed on or introduced in the numerical simulation, the jet shear layer is in actuality continuously stimulated at a very low level as a result of truncation, round-off, and discretization errors (all of which can be characterized as numerical noise—and, in a sense, are analog to environmental background noise in experiments). Among these (random) perturbations, those whose frequency falls within the unstable range for the jet shear layer will draw energy from the mean flow and grow in the streamwise direction, and the other will eventually decay out. For the initially parallel shear layer above at the conditions under consideration, the unstable range is $0 < St < 0.6963$. These growing perturbations interact with the shock-cell structure of the jet plume and thereby generate acoustic waves.

As has already been pointed out, a small (amplitude 10^{-3}) harmonic forcing at the observed screech Strouhal number is imposed on the shear layer at the nozzle lip, where its receptivity is considered the highest, in our computations. This will slightly organize the flow and thereby allow conditional sampling (or phase averaging) techniques to be used to extract wave generation and propagation properties relevant to the screech phenomenon from the numerical computation. In an ideal simulation, the harmonic forcing could be turned off once the self-sustained screech tone has developed through the feedback loop, or might not even be necessary. However, in our simulation, the nozzle lip is of zero thickness and therefore we do not expect the feedback loop to be 'properly closed' at present. This expectation is borne out by the computations and a finite nozzle lip will be used in planned future work.

4.1 Jet Shock-Cell Structure

Experimental results for supersonic jets are often documented in terms of Schlieren pictures. It is straightforward to construct Schlieren graphs from the numerical results without loss of accuracy in view of the nature of the CE/SE method. Fig. 4 shows a comparison of numerical Schlieren (density gradient modulus) contours from the current computations for the initially parallel shear layer case and the experimental Schlieren photograph in [2]. The numerical result is a snapshot of the instantaneous density gradient after about 6 periods of computation from actual startup of the simulation, where a the period is defined in terms of the imposed Strouhal number, *i.e.* $1/St = 1.6949\ldots$. Due to the nature of the Euler solver, there is practically no dissipation in the solution, thus strong vortex roll-up occurs in the shear layers downstream of the shock cells in contrast to the blurred shock cells observed in the experiment. However, the shock cells that have developed so far in the simulation agree quite well with the experimental ones.

4.2 Near-Field Radiating Waves

As have already been alluded to, this highly nonlinear system with discontinuities (shock-cell structure) exhibits wave motion in a rather random fashion. In order that the waves associated with the particular frequency of $St = 0.59$ can be clearly displayed and examined, a conditional sampling technique is applied to the computed data. Using the harmonic forcing as a phase reference, the computed results can be averaged over several periods for any particular phase angle selected. This technique is sometimes referred to as phase averaging. In the present work, this procedure was carried out for 24 phase angles using 50 cycles to construct the averages after the start-up transients propagate out of the computational domain (12-15 cycles). It should be noted that the conditional sampling (or phase averaging) for efficiency is implemented as an integral part of the time marching numerical procedure.

Fig. 5 demonstrates a typical result (one of the 24 phase averages) for the initially parallel shear layer case. It is a combination of isobar contours and numerical Schlieren (moduli of density gradients) contours. In the processing of the numerical data for this figure, the very high level isobar contours, corresponding to hydrodynamic waves around the jet core area are 'cut off' and the 'colors' are appropriately adjusted so that the acoustic waves are clearly displayed. As seen in Fig. 5, these acoustic waves propagate in both upstream and downstream directions separated by a radial line. The first harmonic—waves with half the period or twice the frequency—is expected to be dominant along this dividing line. The acoustic wavelength is about $1.6D$, each shock cell (a pair of shock diamonds) spans about $0.8D$ in the axial direction. These results agree well with experimental results (e.g. [2]) and theoretical predictions (e.g. Seiner [5], Tam [4]).

The remaining phase averages are not included here for brevity, but all 24 can be seen as an animation movie at the web address[1]

www.grc.nasa.gov/WWW/microbus/cese/screech.html

In the animation, it is observed that the first shock cell does not appear move or deform at all, i.e. the shear-layer instability wave is too weak at this location to significantly affect the shock cell. However, it interacts strongly with the shock cells once it has achieved a sufficient amplitude through its streamwise growth, which is evident in the animation by the motions an deformation of the third and fourth shock cells. The deformation and movement of the shock cells are also seen in the experiments [2, 3]. This is, as pointed out by Tam [4], the mechanism by which the acoustic waves involved in broadband shock-associated noise and screech tones are generated and this is also evident in the animation. Furthermore, the fifth shock cell and those further downstream in the animation are so severely deformed that they appear quite different from the first few shock cells.

Fig. 6 is a side-by-side comparison of the computed acoustic field for the case with the artificially spread shear layer and the experimental one [2] for four phase angles. Note that for this comparison, only half of the computational domain ($0 \leqslant x \leqslant 6D$) is shown. Both the experimental and computational data in this figure are phase averaged results. The increment in the phase angle between the different panels is the same for both type of results. However, it is not possible to assign an absolute phase angle to both cases since the phase difference between the 'reference' signals used to obtain the conditional samples in the two cases is not known. Consequently, the panels are arranged in such a way that their phases in a period match the best to each other. It can be observed that the upstream propagating acoustic waves match well with the experimental ones, while the numerical downstream propagation waves appear to be too strong.

Fig. 7 shows the phase averaged pressure fluctua-

[1] A frames version is also available at http://www.grc.nasa.gov/WWW/microbus, which gives access to further CE/SE examples and information.

tions at the nozzle lip at various phase angles during a period. These waves are obviously non-sinusoidal. they contain other frequencies even though the forcing at the nozzle lip is a low-level pure sine wave. Thus, there is feedback to the nozzle lip from the strong shock-cell/instability-wave interactions occurring further downstream.

A simple test was conducted by turning off the artificial perturbation of the shear layer at the jet nozzle after about 50 periods and running an additional ten periods or more. The overall level of the unsteady motion remained about the same. the motion became less organized, and was judged dominated by the natural instability of the shear layer. This implies that the feedback loop is not properly closed at the lip in the present simulation.

4.3 Time-Averaged Flow

As currently implemented. the conditional sampling procedure provides averaged results corresponding to 24 phase angles. The time average results are obtained by averaging over these 24 phase angles.

Fig. 8 depicts time-averaged results for the case of an initially parallel shear layer. Part (a) shows the axial velocity u profiles as well as contours. Spreading of the shear layer due to mixing is evident. Part (b) shows the pressure and density distributions along the center line ($y = 0$). The pressure and density distributions are in qualitative agreement with experimental results. included here for convenience in Parts (c) [5] and (d) [2].

Fig. 9 shows the corresponding time-averaged numerical results for the case of the initially artificially spread shear layer in Parts (a) and (b). The mean shear layer here spreads more than in the previous case. but, somewhat surprisingly, it actually spreads slower than prescribed by its initial condition. Please recall, however, that the initial condition used corresponds to a perfectly expanded jet and. obviously. the under-expanded situation of the actual computation then must lead to a readjustment of the mean shear-layer flow. Also note that the mean pressure and density variations along the center axis attenuate faster than in the previous case.

Fig. 10 compares time-averaged Schlieren graphs corresponding to the two initial conditions for the jet shear layer. Obviously. the shock cell structure in the second case decay faster. but look closer to the experimental one in Fig. 4 than the first one does. The sonic line within the mean shear layer slants slightly more upwards in the second case. allowing the shock cell structure to decay faster. while in the first case, the sonic line is more parallel to the center line thus causing the annular shear layer to act as a better waveguide and. consequently. the shock-cell structure survives longer.

4.4 Power Spectra

The numerical time history is record for a select number of locations in the flow field and later post-processed to obtain spectral information using Fast Fourier Transform (FFT) techniques. Estimates of the power spectral density (PSD) for pressure are shown in Fig. 11. where Part (a) is for the case with the initially parallel shear layer and Part (b) is for the initially artificially spread shear layer. The Figure shows results for three locations at approximately $5D$ distance from the origin (taken to be located at the center axis at the jet exit) for each case. The solid and long-dashed curves are for a polar angle of 61^o and 29^o. respectively, in both cases. The short-dashed curves are for a polar angle of 11^o in Part (a) and 5^o in Part (b). These power spectral density estimates are typical ones for the flow field. Because of the comparatively short time period (about 50 periods) available for the spectral analysis, a trade-off has to be made between the spectral resolution and the reduction in variance of the estimate. Even though somewhat crude. the results shown represents the best balance between these two conflicting requirements.

The short-dashed curves in Fig. 11 represent power spectral densities at or near the shear layers. The forcing Strouhal number ($St = 0.59$) is discernible in these curves. but it is clear that at these locations the unsteady motion is dominated by the natural instability waves of the jet shear layer. The overall level is the highest for these curves since the strong hydrodynamic waves are involved. As the 'observation' point moves away from the vicinity of the shear layer, the overall level will be reduced as the unsteady motion becomes dominated by the generated acoustic waves.

The solid curves in Fig. 11 correspond to a location in the upper left corner of the domain, where acoustic waves dominate the unsteady motion. There are here substantial differences for the two cases. In Part (a) the curve shows that the mixing noise is dominating the unsteady motion, whereas in Part (b) the curve shows a clear peak at the forcing frequency and significant contributions to the acoustic field by broadband shock-associated noise. The mixing-noise level is also somewhat higher in Part (b). It is clear that due to the difference in the shock cell structure (Fig. 10). particularly we believe due to the more rapid decay of the shock-cell structures further downstream. a

much stronger noise field is generated in the second case.

5 Concluding Remarks

In this paper, the recent CE/SE Euler scheme is applied to noise computation for a supersonic shock-containing axisymmetric jet. The advantages of the CE/SE scheme were confirmed in the present simulation. The implementation is 'effortless' in that no special treatment and parameter selections are needed. Many aspects of the computed results are also in good agreement with experimental findings [2, 3]. However, from the literature [4] and our experience herein, it is clear that both the annular shear layer spreading near the jet nozzle and the details of shock-cell structure affect the overall quality of the noise prediction. It is concluded that the sensitivity of our results to the initial shear-layer assumptions is inherent in using an Euler scheme. We plan to apply a CE/SE Navier-Stokes solver, desirably with a large-eddy simulation capability in our further investigation. There is reason to believe that this should not only provide a correctly spreading jet shear layer but should also reduce the amplitude of the downstream propagating acoustic waves. Finally, a self-sustained oscillation, *i.e.* the screech tone, is yet to be achieved in our simulation. The addition of a finite lip of the nozzle coupled with the viscous scheme should rectify this situation. The results will be reported in the future.

The authors wish to thank Dr. J. Panda for fruitful discussions about the jet screech phenomenon.

References

[1] Chang, S. C., "The Method of Space-Time Conservation Element and Solution Element—A New Approach for Solving the Navier-Stokes and Euler Equations," Journal of Computational Physics, v. 119, 295-324 (1995).

[2] Panda, J., "Shock oscillation in underexpanded screeching jets," *J. Fluid Mech.*, v. 363, pp. 173-198 (1998).

[3] Panda, J., "An experimental investigstion of screech noise generation," *J. Fluid Mech.*, v. 378, pp. 71-96 (1998).

[4] Tam, C. K .W., "Supersonic Jet Noise," Ann. Rev. Fluid Mech. v. 27, pp. 17-43 (1995).

[5] Seiner, J. M., "Advances in High Speed jet Aeroacoustics," AIAA Paper 84-2275 (1984).

[6] Tam, C. K. W., "Jet Noise Generated by Large Scale Coherent Motion," NASA RP-1258, pp 311-390 (1991).

[7] Raman G., "Advances in Understanding Supersonic Jet Screech: Review and Perspective," Prog. Aerospace Sci. v. 34, pp. 45-106 (1998).

[8] Cain, A. B., Bower, W. W., Walker, S. H. and Lockwood, M. K. "Modeling Supersonic Jet Screech Part 1: Vortical Instability Wave Modeling," AIAA Paper 95-0506 (1995).

[9] Kerschen, E. J. and Cain, A. B., "Modelling Supersonic Jet Screech Part 2: Acoustic Radiation from the Shock-Vortex Inteaction," AIAA Paper 95-0507 (1995).

[10] Shen, H. and Tam, C. K. W., "Numerical Simulation of the Generation of Axisymmetric Mode Jet Screech Tones," AIAA Paper 98-0283 (1998).

[11] Chang, S. C. and To, W. M., "A Brief Description of a New Numerical Framework for Solving Conservation Laws—The Method of Space-Time Conservation Element and Solution Element," *Proceedings of the Thirteenth International Conference on Numerical Methods in Fluid Dynamics*, Rome, Italy, 1992, M. Napolitano and F. Sabetta, eds., Lecture Notes in Physics 414, Springer-Verlag, pp. 396-400. Also published as NASA TM 105737 (1992).

[12] Chang, S. C., Yu, S. T., Himansu, A., Wang, X. Y., Chow, C. Y. and Loh, C. Y., "The Method of Space-Time Conservation Element and Solution Element—A New Paradigm for Numerical Solution of Conservation Laws", *Computational Fluid Dynamics Review*, eds. M. M. Hafez and K. Oshima, Wiley (1997).

[13] Chang, S.-C., Wang, X.-Y. and Chow, C.-Y., "The Space-Time Conservation Element and Solution Element Method—A New High Resolution and Genuinely Multidimensional Paradigm for Solving Conservation Laws, Part I: The Two-Dimensional Time-Marching Schemes," NASA TM-1998-208843 (1998). Also to appear in J. Comp. Phys. (1999).

[14] Loh, Ching Y., Hultgren, Lennart S. and Sin-Chung Chang, "Computing Waves in Compressible Flow Using the Space-Time Conservation Element Solution Element Method," AIAA Paper 98-0369 (1998).

[15] Loh, C. Y., Hultgren, L. S., Chang, S.-C. and Jorgenson, P. C. E., "Vortex Dynamics Simulation in Aeroacoustics by the Space-Time Conservation Element Solution Element Method." AIAA Paper 99-0359 (1999).

[16] Yu, S. T. and Chang, S. C., "Treatment of Stiff Source Terms in Conservation Laws by the Method of Space-Time Conservation Element and Solution Element", AIAA Paper 97-0435 (1997).

[17] Morris, P. J. and Tam, C. K. W., AIAA Paper 77-1351 (1977).

[18] Loh, C. Y., Chang, S. C., Scott, J. R., and Yu, S. T., "Application of the Method of Space-Time Conservation Element and Solution Element to Aeroacoustics Problems." presented at 6th International Symposium of CFD, Lake Tahoe, California (1995).

[19] Loh, C. Y., Chang, S. C., Scott, J. R., and Yu, S. T., "The Space-Time Conservation Element Method—A New Numerical Scheme for Computational Aeroacoustics ", AIAA Paper 96-0276 (1996).

[20] Loh, C. Y., Chang, S. C. and Scott, J. R., "Computational Aeroacoustics via the Space-Time Conservation Element/Solution Element Method", AIAA Paper 96-1687 (1996).

[21] Chang, S. C., Himansu, A., Loh, C. Y., Wang, X. Y., Yu, S.-T. and Jorgenson, P. C. E. "Robust and Simple Non-Reflecting Boundary Conditions for the Space-Time Conservation Element and Solution Element Method", AIAA Paper 97-2077 (1997).

[22] Chang, S. C., Loh, C. Y. and Yu, S. T., "Computational Aeroacoustics via a New Global Conservation Scheme", *Proceedings of the 15th International Conference on Numerical Methods in Fluid Dynamics*, eds. P. Kutler, J. Flores and J.-J. Chattot, June 24-28, 1996, Monterey, CA (1997).

[23] Wang, X.Y., Chow,C.Y. and Sin-Chung Chang, "Numerical Simulation of Gust Generated Aeroacoustics in a Cascade Using the Space-Time Conservation Element Solution Element Method", AIAA Paper 98-0178 (1998)

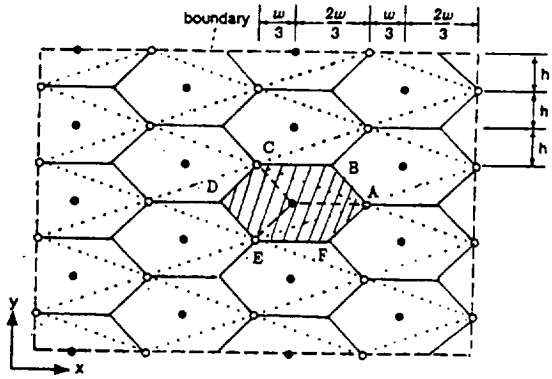

Figure 1: The spatial node locations of the grid sets Ω_1 (hollow circles) and Ω_2 (solid circles), showing the hexagon structure of $CE^{(1)} = CE_1^{(1)} - CE_2^{(1)} - CE_3^{(1)}$ with $\Omega_{1,}$; shaded hexagon corresponding to Fig. 2(a) and x-axis being the axis of symmetry.

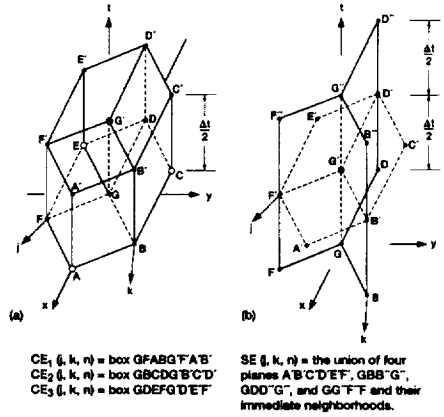

Figure 2: (a) Conservation element $CE_1^{(1)}$ and (b) solution element $SE_1^{(1)}$

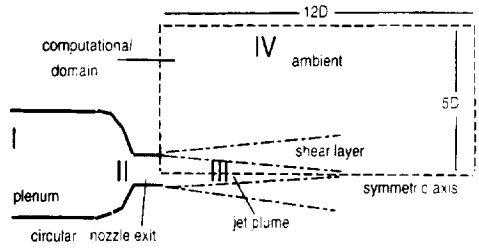

Figure 3: Sketch of the jet noise problem: only Regions III and IV are included in the computational domain.

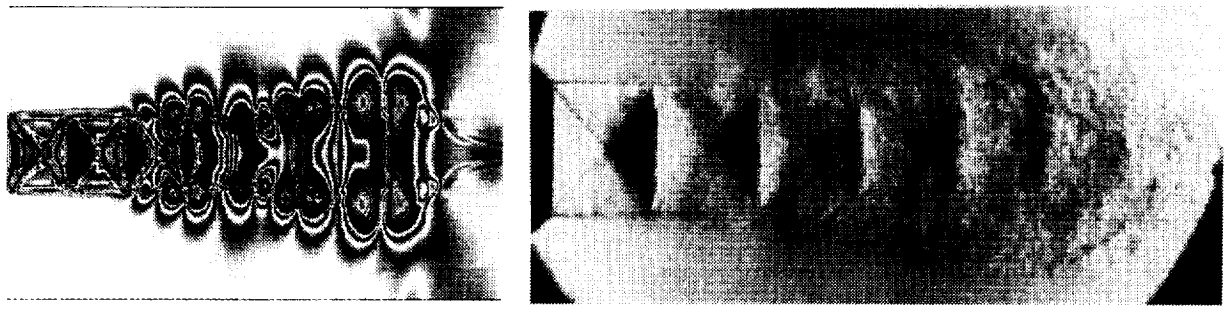

Figure 4: Comparison of numerical Schlieren graph (instantaneous snapshot, left panel) and the experimental time averaged Schlieren graph (right panel); showing excellent agreement of the first few shock cells.

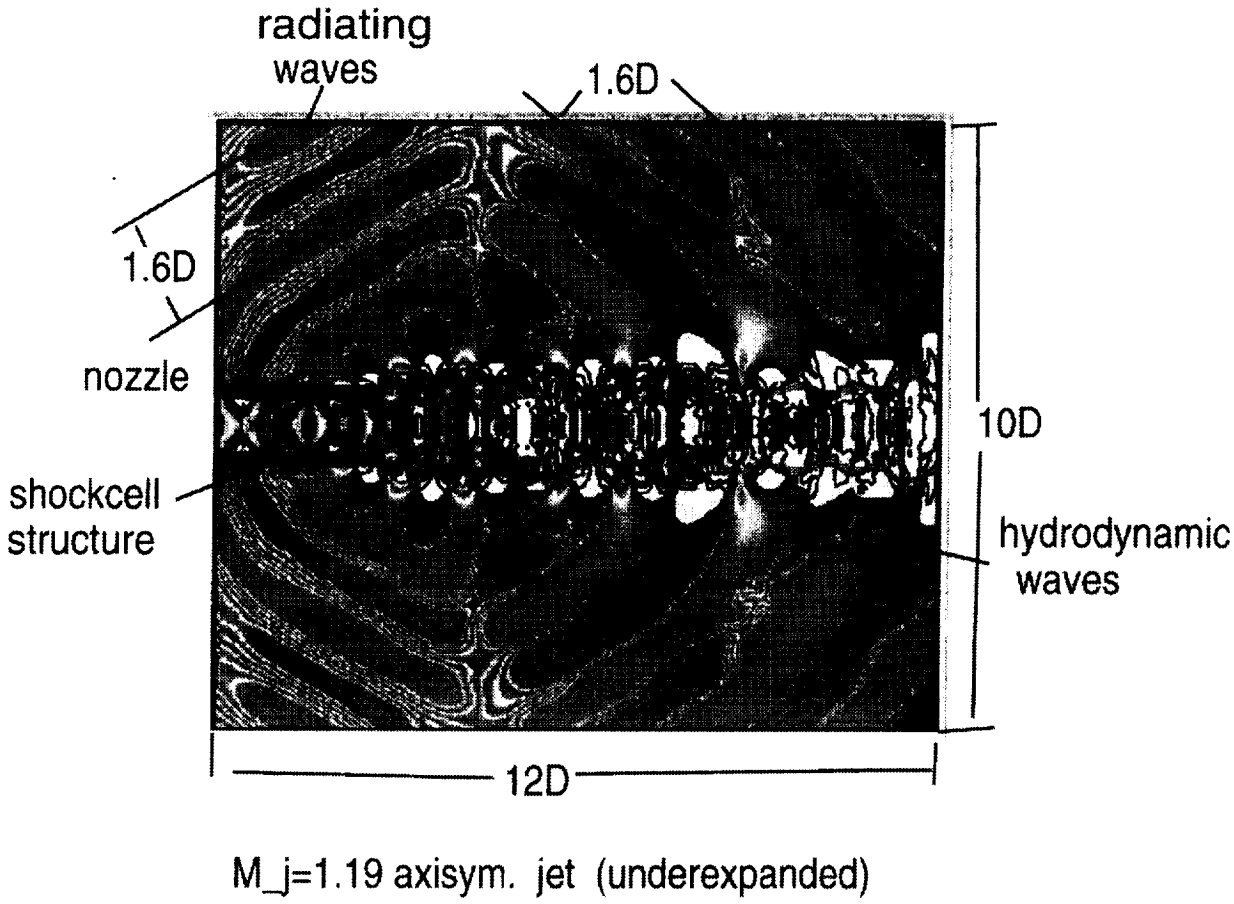

Figure 5: Typical phase averaged isobars and numerical Schlieren pictures (parallel initial shear layer). showing radiating waves and the shock-cell structure.

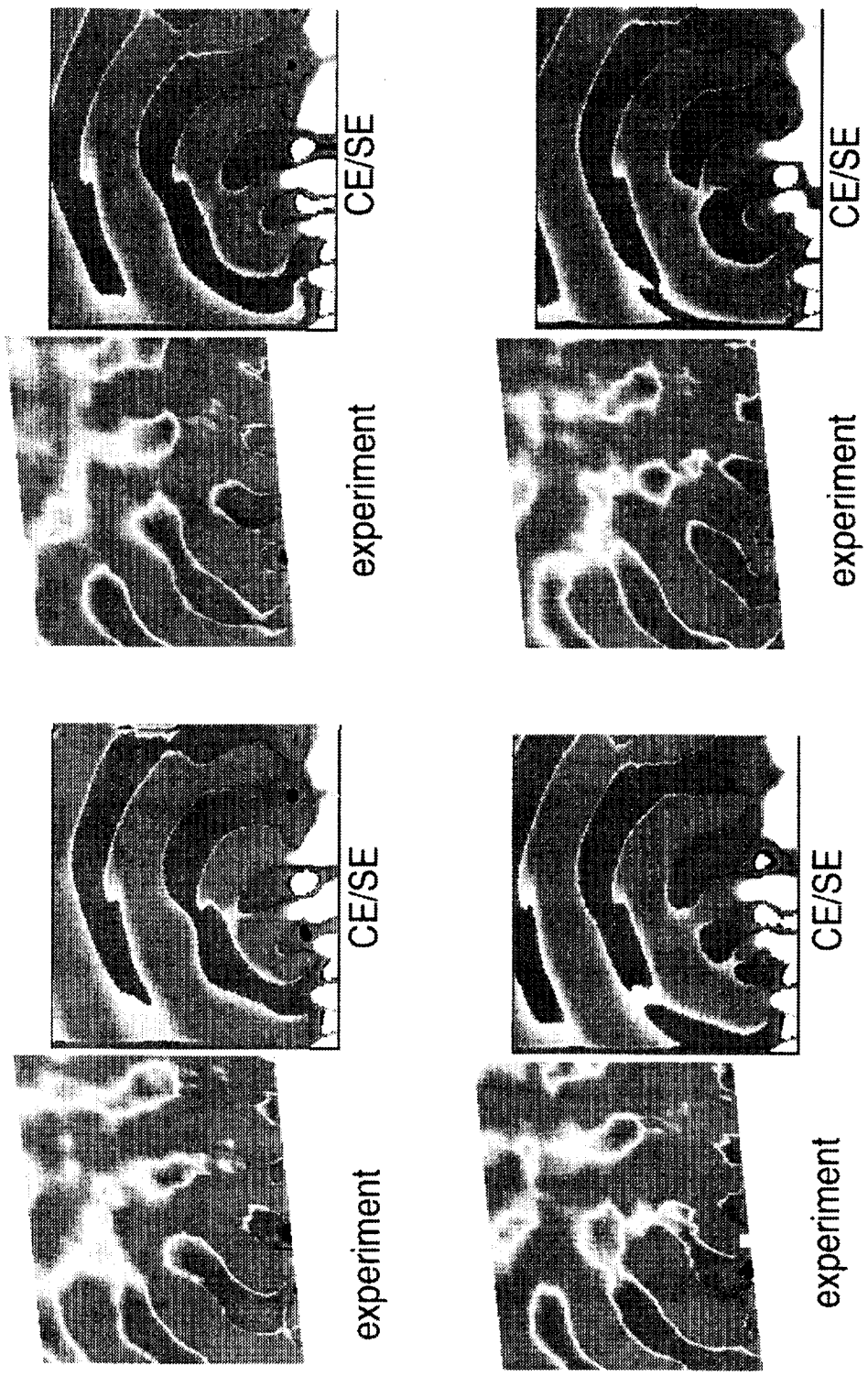

Figure 6: Comparison of upstream propagating wave patterns with experimental screech waves for phase phase angles (artificially spread initial shear layer).

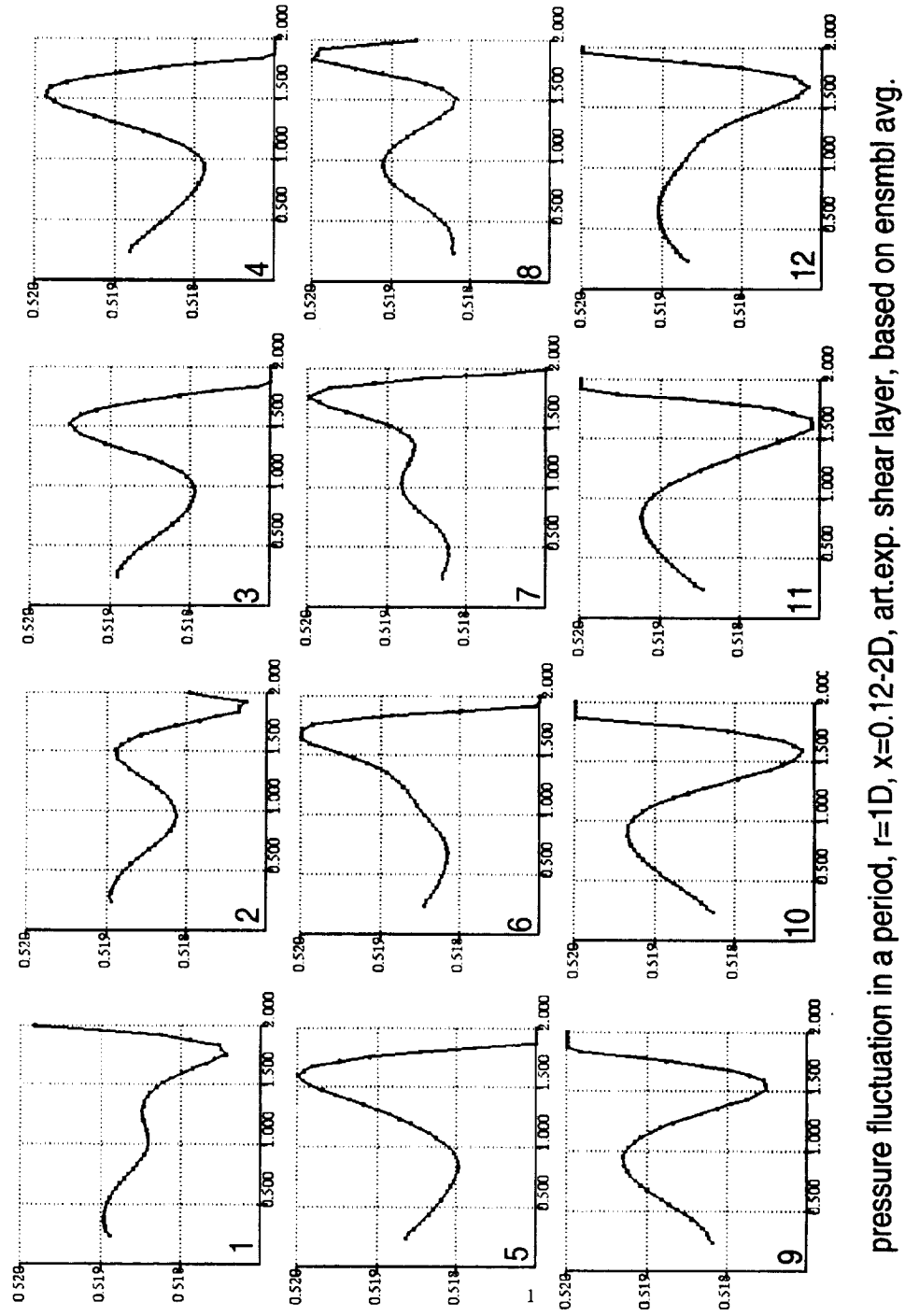

Figure 7: Pressure fluctuation in a period for 12 phase angles near the jet nozzle ($r = 1D, 0.12 \leqslant x \leqslant 2D$), showing non-sinusoidal wave motion.

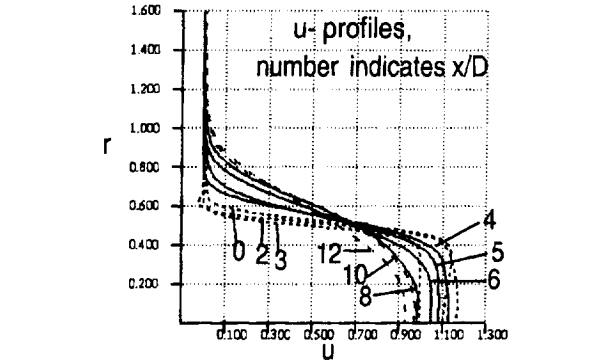

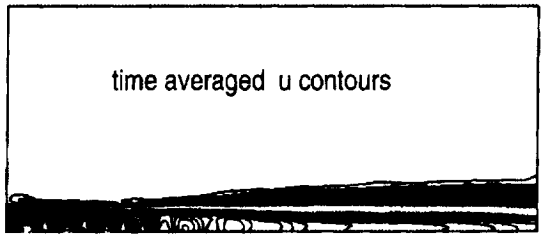

time averaged u contours and profiles (simple shear layer)

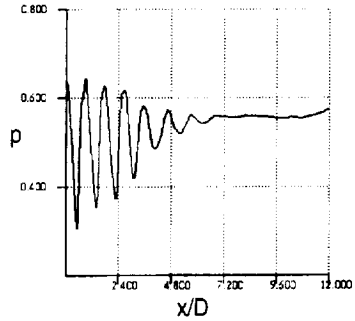

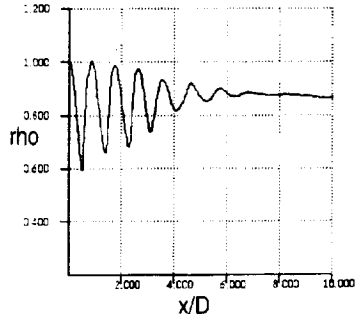

time averaged p and rho at axis
(simple shear layer)

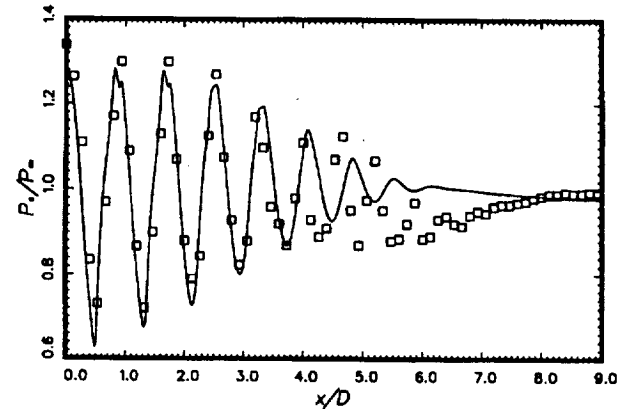

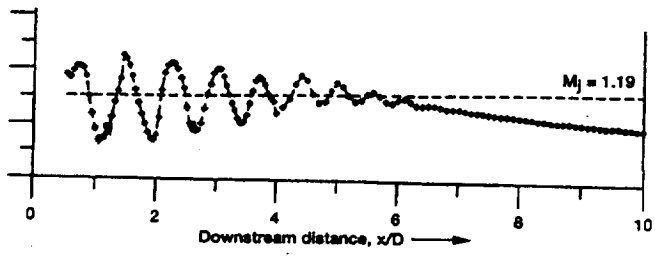

Figure 8: Time-averaged u profiles and contours; time averaged p and ρ along x-axis; experimental and computed result by others (parallel initial shear layer).

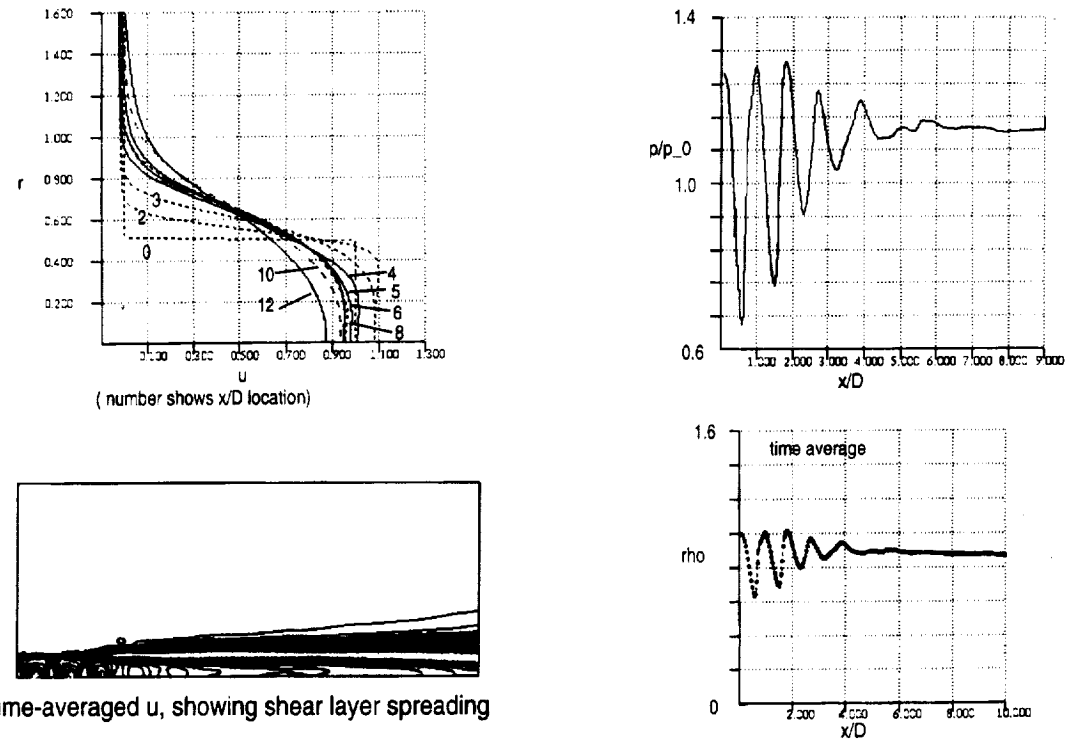

Figure 9: Time-averaged u profiles and contours; time averaged p and ρ along x-axis (artificially spread initial shear layer).

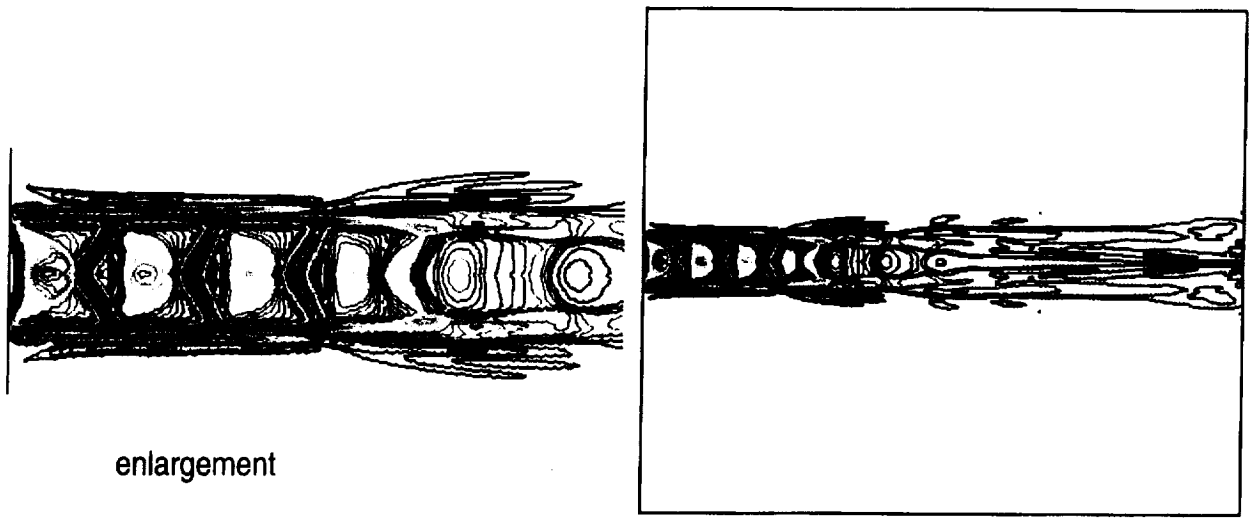

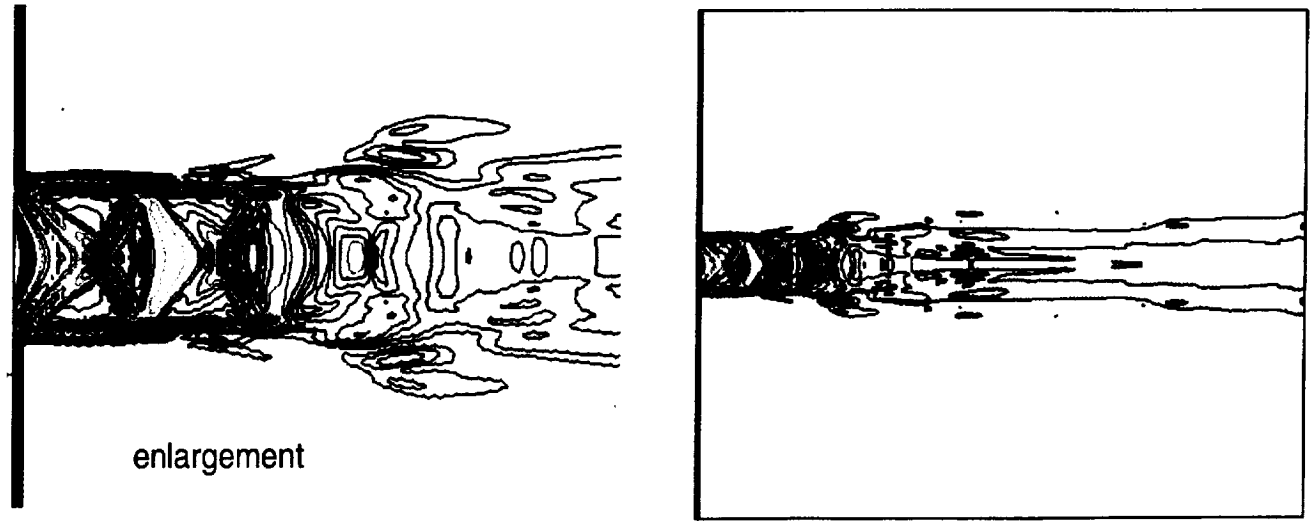

Figure 10: Time-averaged numerical Schlieren pictures, showing shock cell structures: (a) parallel initial shear layer; (b) artificially spread initial shear layer.

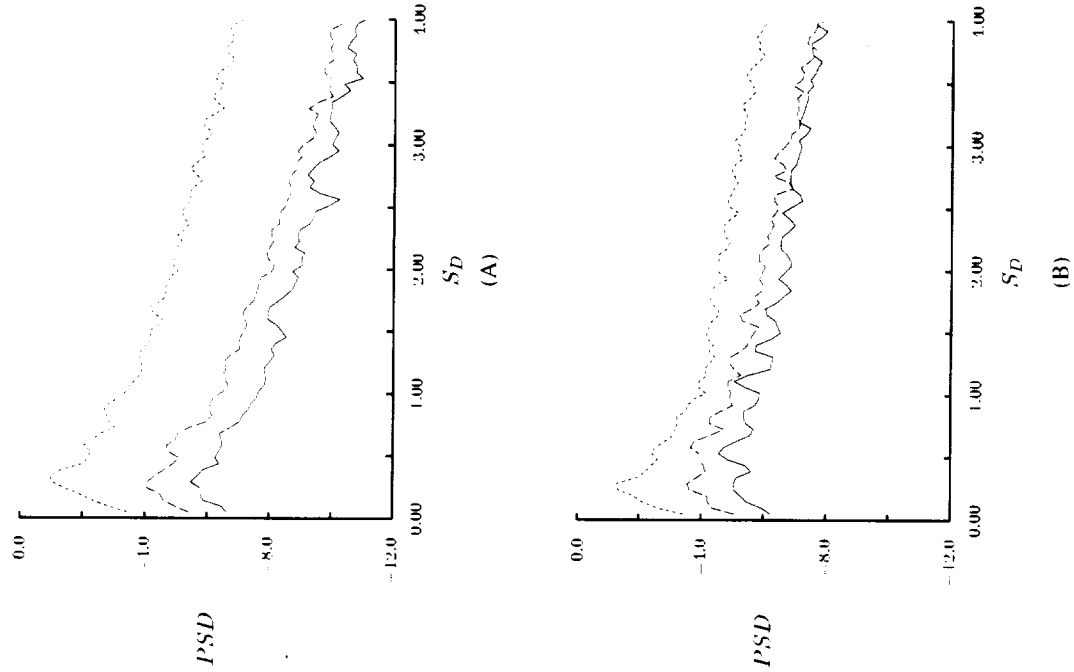

Figure 11: Power spectral density (PSD) for the pressure versus Strouhal number: (a) parallel initial shear layer, (b) artificially spread initial shear layer; showing mixing noise and broadband shock-associated noise.

REPORT DOCUMENTATION PAGE

Form Approved
OMB No. 0704-0188

1. AGENCY USE ONLY (*Leave blank*)	2. REPORT DATE	3. REPORT TYPE AND DATES COVERED
	December 1999	Technical Memorandum

4. TITLE AND SUBTITLE

Noise Computation of a Shock-Containing Supersonic Axisymmetric Jet by the CE/SE Method

5. FUNDING NUMBERS

WU-522-81-11-00

6. AUTHOR(S)

Ching, Y. Loh, Lennart S. Hultgren, Sin-Chung Chang, and Philip C.E. Jorgenson

7. PERFORMING ORGANIZATION NAME(S) AND ADDRESS(ES)

National Aeronautics and Space Administration
John H. Glenn Research Center at Lewis Field
Cleveland, Ohio 44135-3191

8. PERFORMING ORGANIZATION REPORT NUMBER

E-12029

9. SPONSORING/MONITORING AGENCY NAME(S) AND ADDRESS(ES)

National Aeronautics and Space Administration
Washington, DC 20546-0001

10. SPONSORING/MONITORING AGENCY REPORT NUMBER

NASA TM—1999-209658
AIAA-2000-0475

11. SUPPLEMENTARY NOTES

Prepared for the 38th Aerospace Sciences Meeting and Exhibit sponsored by the American Institute of Aeronautics and Astronautics, Reno, Nevada, January 10–13, 2000. Ching Y. Loh, Taitech Inc., Cleveland, Ohio 44135; Lennart S. Hultgren, Sin-Chung Chang, and Philip C.E. Jorgenson, NASA Glenn Research Center. Responsible person, Philip C.E. Jorgenson, organization code 5880, (216) 433–5386.

12a. DISTRIBUTION/AVAILABILITY STATEMENT

Unclassified - Unlimited
Subject Category: 71 Distribution: Nonstandard

This publication is available from the NASA Center for AeroSpace Information, (301) 621–0390.

12b. DISTRIBUTION CODE

13. ABSTRACT ***(Maximum 200 words)***

The space-time conservation element solution element (CE/SE) method is employed to numerically study the near-field of a typical under-expanded jet. For the computed case—a circular jet with Mach number $M_j = 1{:}19$—the shock-cell structure is in good agreement with experimental results. The computed noise field is in general agreement with the experiment, although further work is needed to properly close the screech feedback loop.

14. SUBJECT TERMS

Space-time conservation element and solution element method, Aeroacoustics, Space-time flux conservation

15. NUMBER OF PAGES

21

16. PRICE CODE

A03

17. SECURITY CLASSIFICATION OF REPORT	18. SECURITY CLASSIFICATION OF THIS PAGE	19. SECURITY CLASSIFICATION OF ABSTRACT	20. LIMITATION OF ABSTRACT
Unclassified	Unclassified	Unclassified	